



Cite this: *RSC Adv.*, 2025, **15**, 50019

## Recent advances in porous graphitic frameworks: a critical mini-review

Minh Kim Nguyen,<sup>a</sup> Ha Huu Do,<sup>bc</sup> Nguyen Tien Tran  <sup>\*de</sup> and Young-Chul Lee  <sup>\*f</sup>

Porous graphitic frameworks (PGFs) represent a rapidly maturing class of  $sp^2$ -carbon architectures that reconcile the traditionally antagonistic requirements of very-high surface area, hierarchical mass-transport pathways, and metallic-level electronic conductivity. This mini-review critically surveys the latest advances in their bottom-up construction, from hard-templated and chemical-vapor-deposited networks to emerging inside-out activation-graphitization protocols. This review also correlates these synthetic routes with key structural attributes, surface area, pore-size distribution, and graphitic domain continuity, and elucidates their role in providing exceptional electrical, thermal, and mechanical performance metrics. Application case studies include high-rate supercapacitors, single-atom electrocatalysts, Ångström-precision gas-separation membranes, chemiresistive sensors, and high-capacity adsorbents. Data-driven process control, molten-salt-mediated doping, and additive manufacturing are expected to deliver application-specific PGFs at scale, while advanced functionalization strategies decouple active-site chemistry from bulk conductivity. Collectively, the combination of sustainable synthesis, tunable nanochemistry, and wide applications makes PGFs an effective material platform for next-generation energy, environmental, and electronic technologies.

Received 13th October 2025  
 Accepted 5th December 2025

DOI: 10.1039/d5ra07821k  
[rsc.li/rsc-advances](http://rsc.li/rsc-advances)

### 1. Introduction

Porous graphitic architectures (PGFs) are a new class of carbonaceous materials, which possess a high surface area, the tunable porosity of conventional activated carbons with long range  $\pi$  conjugation, and the crystallographic order of graphitic domains. This combined structural motif directly addresses the long-standing bottlenecks in electrochemical and catalytic technologies, namely, slow charge transport and mass transfer, by providing continuous  $sp^2$  carbon highways through an open-pore network. The rapidly growing volume of the literature on 3D porous graphene architectures for energy storage reflects the growing strategic importance of this design paradigm.<sup>1</sup>

At the molecular level, PGFs are built from perfectly annulated aromatic backbones, in which rigid ladder-like linkages fix neighboring benzene or heteroaromatic units to planar sheets. Periodic voids are incorporated either by intrinsic ring fusion or sacrificial templating. The demonstration of dynamic covalent

$C=N$  exchange in pyrazine rings by Li *et al.* (2020) was a breakthrough, allowing for crystalline PGF, providing a template for the attainment of in-plane order under relatively mild hydrothermal conditions, and the discovery of reversible bond formation as an essential function in error correction during framework development.<sup>2</sup> Follow-up ladder polymer strategies have been developed based on this concept to create conjugated porous networks with redox-active backbones that can be systematically optimized for battery electrodes and other platforms for charge storage.<sup>3</sup>

The resulting materials possess a set of properties that are difficult to obtain simultaneously using conventional carbons. Electrical conductivities above  $10\text{ S cm}^{-1}$ , Brunauer–Emmett–Teller (BET) surface areas always greater than  $1\,000\text{ m}^2\text{ g}^{-1}$ , and excellent thermal and chemical stability due to graphitic bonding. Recent studies have emphasized how these properties translate into functional advantages. For instance, metal-organic frameworks (MOF)-derived PGFs with spinel  $\text{NiFe}_2\text{O}_4$  nanoparticle decorations exhibit remarkably faster perchlorate degradation rates by synergistically bridging conductive carbon highways and rich catalytic interfaces,<sup>4</sup> while Kr adsorption research now allows quantitative edge plane density mapping of graphitic carbons, giving a metrology for defect chemistry correlation with adsorption or electrocatalytic activity.<sup>5</sup>

Despite these developments, significant knowledge gaps remain in the literature. However, scalable synthesis routes that balance crystallinity, heteroatom incorporation, and hierarchical pore development remain elusive. *In situ* characterization

<sup>a</sup>Department of Nanoscience and Technology Convergence, Gachon University, Gyeonggi-do 13120, South Korea

<sup>b</sup>NTT Hi-Tech Institute, Nguyen Tat Thanh University, Ho Chi Minh City, Vietnam

<sup>c</sup>Nguyen Tat Thanh University Center for Hi-Tech Development, Saigon Hi-Tech Park, Ho Chi Minh City, Vietnam

<sup>d</sup>Center for Advanced Chemistry, Institute of Research and Development, Duy Tan University, Da Nang 550000, Vietnam. E-mail: [trannguyentien@duytan.edu.vn](mailto:trannguyentien@duytan.edu.vn)

<sup>e</sup>Faculty of Natural Sciences, Duy Tan University, Da Nang 550000, Vietnam

<sup>f</sup>Department of Bionanotechnology, Gachon University, Gyeonggi-do 13120, South Korea. E-mail: [dreamdbs@gachon.ac.kr](mailto:dreamdbs@gachon.ac.kr)



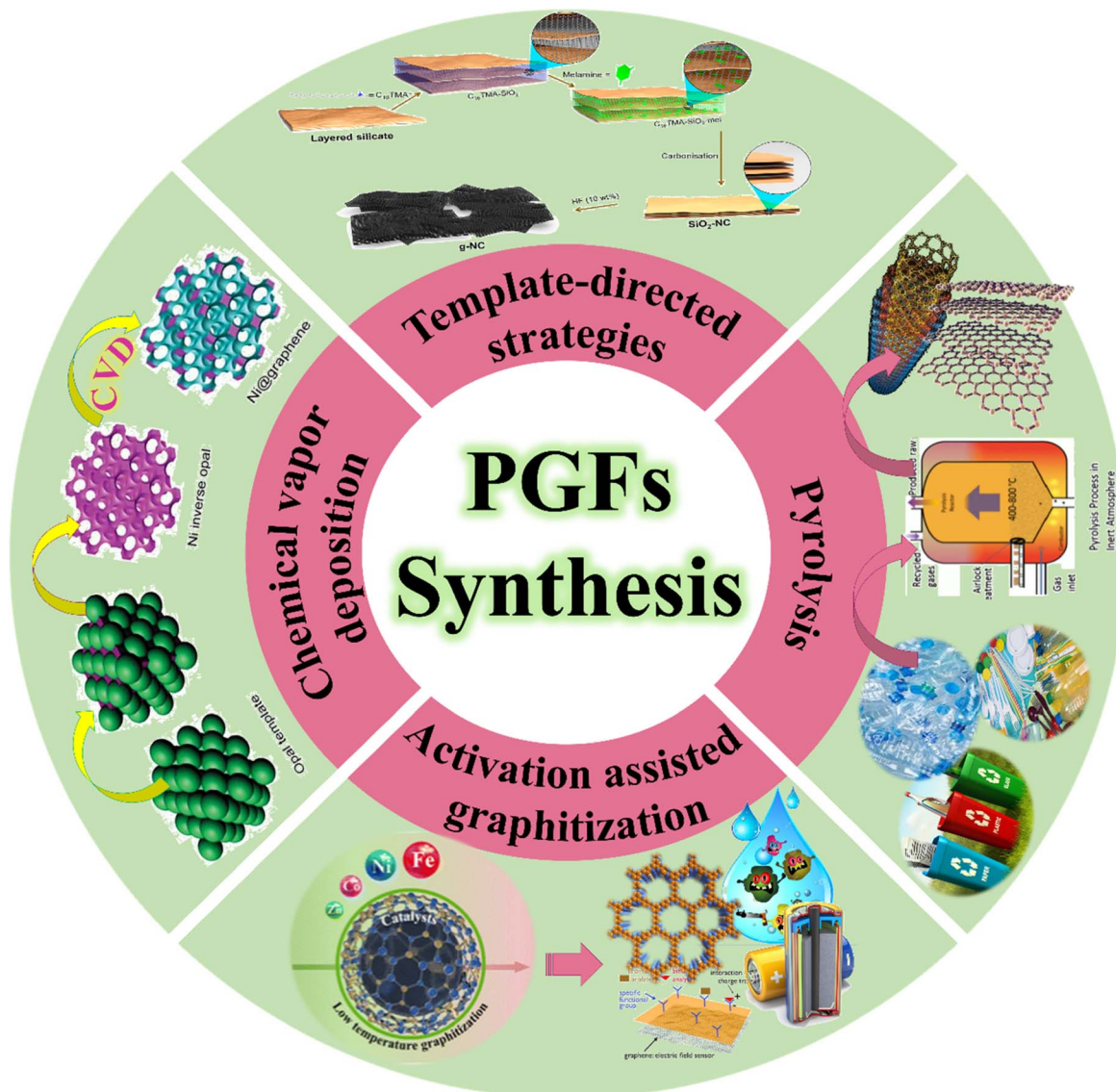


Fig. 1 PGFs synthesis techniques.

techniques capable of resolving ion or molecule transport within sub-nanometer graphitic channels are only beginning to be developed. This mini-review focuses on the most recent synthetic advances (Fig. 1). Besides, it also summarizes structural characterization methods, emergent behavior, and application horizons of PGFs toward distilling structure–function relationships to guide the rational design of future graphitic porous materials.

## 2. Synthesis methods

Porous graphitic frameworks can be synthesized *via* several conceptual routes that differ in how graphitic domains nucleate, how pore geometry is templated, and how heteroatom chemistry is incorporated. Accordingly, three different synthesis approaches groups can be mentioned. Accordingly, soft-templated or supramolecular-templated routes, in which

micellar, block-copolymer, or hydrogen-bonded assemblies are used to pre-organize carbon or nitrogen-rich precursors into meso-structured domains that are subsequently carbonized.<sup>6–9</sup> Hard-templated and CVD-assisted routes, where rigid silica, polymer, or 3D graphene scaffolds support the formation of hierarchical pore networks coupled with graphitization.<sup>10–12</sup> And MOF/COF-derived or salt-assisted pyrolysis strategies, in which reticular frameworks or supramolecular mixed matrices are transformed into N-doped graphitic carbons with atomically dispersed metals and well-defined micro/mesopores.<sup>13,14</sup>

Hard-templating (*e.g.*, silica, layered silicates, MgO) provides the high geometric precision and often forms ordered or pseudo-ordered mesopores after template removal, as demonstrated in recent studies producing graphitic nitrogen-enriched carbons using exfoliable silicate platelets as sacrificial scaffolds.<sup>6</sup> Conversely, soft-templates, such as block-copolymers, supramolecular micelles, and ionic surfactant assemblies,

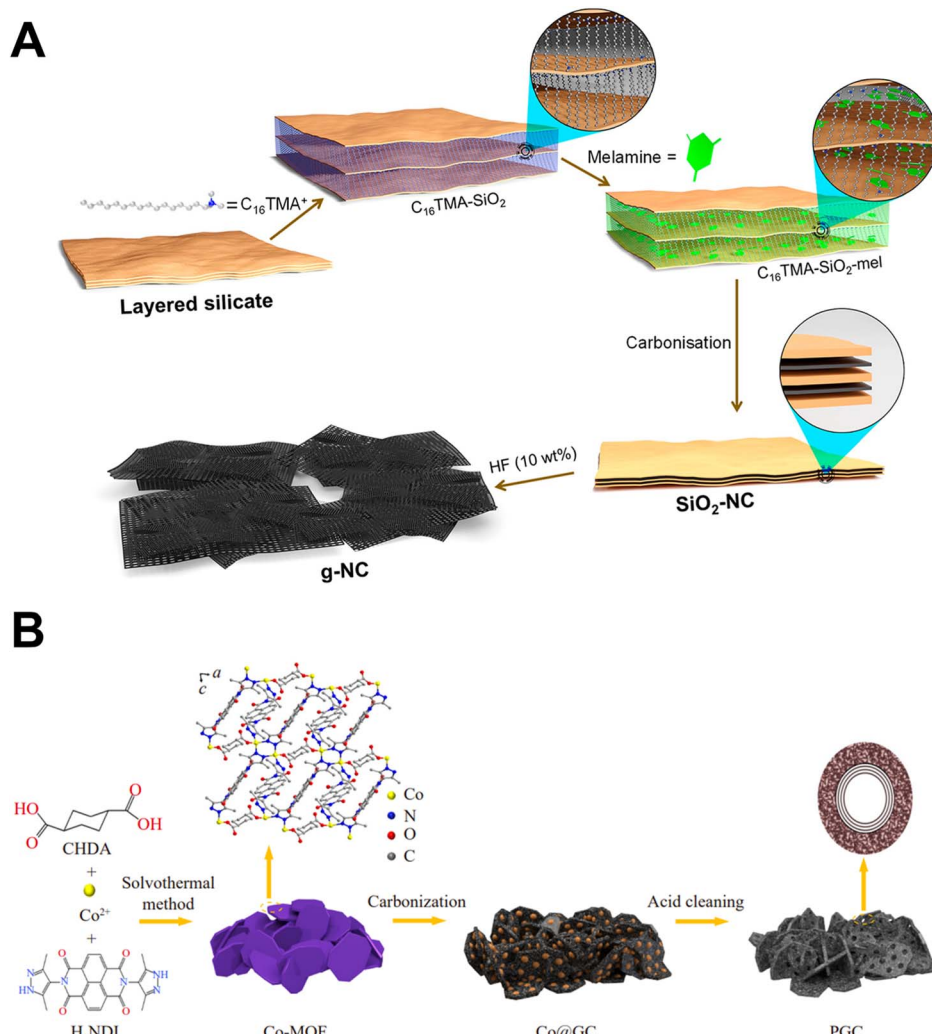


Fig. 2 (A) Synthesis scheme for g-NC using hard templating.<sup>6</sup> Reuse permission from Doustkhah *et al.* (2023)<sup>6</sup> by American Chemical Society. (B) Synthesis of porous graphitic carbons from Co-MOF precursors.<sup>29</sup> Reuse permission from Chu *et al.* (2024)<sup>29</sup> by Springer Nature, under a Creative Commons Attribution 4.0 International License (<https://creativecommons.org/licenses/by/4.0/>).

enable large-area meso-structure formation without corrosive etching, as shown in mesoporous graphitic carbons derived from Pluronic-directed assemblies.<sup>15</sup> CVD approaches provide atomic-level control of  $\text{sp}^2$  domain and allow heteroatom integration, consistent with reports using methane decomposition on  $\text{MgO}$  microspheres to yield double-layer graphitic membrane which possessed approximated BET of  $1500 \text{ m}^2 \text{ g}^{-1}$ .<sup>8</sup> Finally, pyrolysis-based graphitization of MOFs, conjugated polymers, biomass, and supramolecular matrices has become the flexible route for scalable PGF production, especially when combined with catalytic graphitization (Ni, Fe, Co) or activation (K-based, molten salts).<sup>16-18</sup> These routes have recently achieved hierarchically porous carbons with controllable micro/mesopore ratios, graphitization indices, and electrical conductivities reaching  $10 \text{ S cm}^{-1}$ .<sup>9,13,19</sup>

Recent reports on nitrogen-doped porous graphitic carbon prepared by layered double hydroxide templating,<sup>6</sup> conjugated-polymer-derived 3D porous graphitic carbons,<sup>7</sup> and 3D porous

graphene/carbon nanocage architectures<sup>8</sup> represent the first two families, whereas Ni-MOF-derived Ru-N<sub>4</sub> single-atom catalysts,<sup>13</sup> ZIF-derived Zn single-atom-embedded carbon molecular sieves,<sup>9</sup> and NaCl-assisted ZIF-8 carbonization towards porous N-doped carbons hosting precious-metal single atoms<sup>19</sup> illustrate the third family. In parallel, g-C<sub>3</sub>N<sub>4</sub>-type porous graphitic frameworks (e.g., mesoporous g-C<sub>3</sub>N<sub>4</sub> nanosheets and heterostructures) are classified as nitrogen-rich analogues that share similar synthetic soft-templating, defect/dopant engineering, and hierarchical morphology control.<sup>20-23</sup> However, they operate primarily as semiconducting photocatalysts rather than purely conductive carbons.<sup>10,24-26</sup>

## 2.1. Template-directed strategies

Hard templating is the most structurally deterministic method for obtaining porous graphitic frameworks (PGFs). The recent work of Doustkhah *et al.* (2023) used exfoliable 2D layered silicate platelets as sacrificial templates.<sup>6</sup> Pyrolysis of a melamine-

cetyltrimethyl-ammonium composite and carbonization–activation process of chitosan/polyethylene glycol (PEG) blend or melamine–resorcinol–formaldehyde (M–R–F) co-polymeric microspheres could provide nitrogen-rich graphitic carbons with a micro/mesopore-architectures that replicated the inter-layer gallery.<sup>6,27,28</sup> Density functional analysis confirmed graphitic N as the thermodynamic sink, accounting for the material's 90% capacitance retention up to 10 000 cycles (Fig. 2A).<sup>6</sup> In a self-templated complementary counterpart, nano  $\text{CaCO}_3$  was utilized to form pores and serve as an *in situ*  $\text{CO}_2$  source to prevent sheet restacking. The resulting  $\text{CaCO}_3$ /coffee ground hybrid had a discharge of 760  $\text{mA h g}^{-1}$  after 100 LIB cycles, illustrating a pathway for using transient inorganic domains to control porosity and heteroatom doping simultaneously.<sup>1</sup> Despite this success, mineral template removal (thermal volatilization or acid leaching) remains energy-intensive and limits scalability. Therefore, the field is moving toward bio-templated or melt-salt approaches that integrate template decomposition with graphitization.

Besides, soft-template strategies use surfactant assemblies, block-copolymer micelles, supramolecular hydrogen-bonded networks, or ionic liquid–polymer co-assemblies—are capable of producing mesoporous carbons with ordered or semi-ordered pore lattices without the corrosive template etching required in hard templating. Recent reviews on mesoporous graphitic/non-graphitic carbons<sup>11,12</sup> highlight how Pluronic F127, P123, CTAB, and related amphiphiles can direct precursor polymerization prior to carbonization, yielding tunable 2–50 nm mesopores with high pore volumes and uniform distributions. In addition, soft-templated graphitic carbon nitride ( $\text{g-C}_3\text{N}_4$ ) systems, particularly mesoporous or doped  $\text{g-C}_3\text{N}_4$ , follow analogous supramolecular-assembly principles and are widely employed in photoactive or redox applications.<sup>10,20–26</sup>

Hard-templated PGFs, such as silica, layered silicates,  $\text{CaCO}_3$ , and  $\text{MgO}$ , often exhibit high graphitic ordering and well-defined mesopore channels after template removal, as confirmed through Raman  $I_{\text{D}}/I_{\text{G}}$  ratios, XRD, and TEM analyses. They produce pore geometries that directly replicate the template lattice. Representative examples include exfoliable silicate-templated nitrogen-rich graphitic carbons<sup>6</sup> and  $\text{MgO}$ -derived graphenic nanocages.<sup>8</sup> By contrast, soft templates, while generally less crystalline, typically generate ordered mesopores and offer enhanced dopant homogeneity and better control over mesopore dimensions due to the uniformity of micellar domains. However, they lack rigid anchoring points during carbonization. Thereby, these aspects make them advantageous for scalable synthesis and facile doping, yet more susceptible to framework shrinkage. Soft-templated mesoporous carbons and mesoporous  $\text{g-C}_3\text{N}_4$  demonstrate these trade-offs, and their common structural motifs have now been explicitly discussed using recent literature.<sup>14,21,22</sup>

## 2.2. Chemical vapor deposition on 3D scaffolds

Chemical vapor deposition (CVD) offers atomic-level control of the graphitic layer growth and separates carbon nucleation from pore formation. Zhu *et al.* (2019) demonstrated a fluidized

bed CVD process where  $\text{CH}_4$  decomposes on  $\text{MgO}$  microspheres at 950 °C to form a conformal double-layer graphene skin that preserves the sacrificial template's nest like microporosity. After  $\text{MgO}$  removal, the scaffold exhibited a BET surface area of 1460  $\text{m}^2 \text{ g}^{-1}$  and tolerated 1560  $\text{mA h g}^{-1}$  in LIB anodes.<sup>1,8</sup> The gas phase nature of CVD enables seamless incorporation of heteroatom dopants (e.g.,  $\text{B}_2\text{H}_6$ ,  $\text{NH}_3$ ) or catalytic nanoparticles onto growth but is constrained by throughput by residence time and precursor consumption, inefficiencies of limitations addressed by microwave plasma and roll to roll aerosol CVD reactors.

## 2.3. Pyrolysis of pre-organized organic precursors

The direct carbonization of covalent organic frameworks, MOFs, and biomass produces PGFs whose pore structures are imprinted in the precursor. Chu *et al.* carbonized a triply interpenetrated Co-MOF at 1300 °C to produce PGC 1300, featuring a high graphitization index and interconnected 1–5 nm mesopores. The anode delivered 128.5  $\text{mA h g}^{-1}$  at 3.2  $\text{A g}^{-1}$  in lithium-ion capacitors and retained 91.6% capacity after 10 000 cycles (Fig. 2B).<sup>29</sup> Parallel biomass-derived routes leverage the inherent hierarchical routes. Precursors of peanut shell and pumpkin skin, *via* two stage calcination, yield graphitic carbons with surface area  $>2\,000 \text{ m}^2 \text{ g}^{-1}$  and oxygen functionalities facilitating K-ion adsorption.<sup>30–32</sup> Significant bottlenecks include precursor heterogeneity and the need for high temperatures (>1200 °C) for  $\text{sp}^2$  ordering. Catalytic graphitization using Fe, Ni, or Co salts is more commonly used to minimize energy footprint (Table 1).

## 2.4. Activation-assisted graphitization

Physical or chemical activation increases the number of micropores and causes defects but traditionally at the cost of conductivity. Zhao and Zhang solved this problem using an *in situ* activation–graphitization process. Atomically dispersed K (activator) and Fe (graphitization catalyst) in precursors of potassium/ferric citrate lead to “inside out” growth of pores along with ordering of the lattice to give hierarchical PGF with 322  $\text{F g}^{-1}$  and 101% capacitance retention after 15 000 cycles.<sup>34</sup> Environmentally friendly activating agents such as  $\text{KHCO}_3$  and  $\text{Na}_2\text{CO}_3$ , and molten salt media now replace corrosive  $\text{KOH}/\text{ZnCl}_2$ , suppressing equipment corrosion while enabling closed loop recovery of salt. However, precise control of the one-step activation pore size distribution is still inaccessible, stimulating *operando* small-angle X-ray scattering research to correlate gas and pore evolution in real time.

## 2.5. Advantages and disadvantages across various aspects

**2.5.1. Energy cost.** Hard-templated carbons and MOF-derived PGFs typically require 800–1500 °C to achieve graphitic ordering, as demonstrated in recent high-temperature carbonization of Co-MOF precursors.<sup>29</sup> CVD also operates in the 900–1100 °C regime, consuming additional energy within gas-phase reactors, thereby increasing overall operational cost.<sup>8</sup> In contrast, molten-salt graphitization has recently achieved graphitic ordering at significantly lower temperatures (~900 °C)

Table 1 The various synthesis methods, properties, and the applications of PGFs materials

Method	Precursors	Conditions	Product	Applications	Ref.
Hard templating	Layered silicate, melamine and cetyltrimethyl ammonium (C16TMA)	Heated at 800 °C	g-NC (C <sub>6.3</sub> H <sub>3.6</sub> N <sub>1</sub> O <sub>1.2</sub> )	Electrocatalytic, supercapacitance	6
Hard templating	Coffee ground, calcium carbonate and iron nitrate	Carbonized at 750 °C	NC3320	Electrochemical	1
CVD	CH <sub>4</sub> and MgO catalyst	950 °C in fluidized bed reactor	S/PHG-5	Electrochemical	8
Pyrolysis	Co-MOF	Pyrolysis at 900–1500 °C	PGC-x	Electrochemical, lithium-ion capacitor	29
Pyrolysis	Pumpkin skin powder	Pyrolysis at 900 °C	GHPC	Electrochemical, supercapacitors	30
Pyrolysis	K <sub>2</sub> CO <sub>3</sub> , g-C <sub>3</sub> N <sub>4</sub>	Pyrolysis at 700–900 °C	ONPC-900	Electrochemical, supercapacitors	33
Pyrolysis- flash Joule heating	Sawdust, bamboo, and rice straw	Vacuum desiccator ~0.6 psi, 200 V, 50 Hz	FG	Catalyzed hydrogenation, photothermal conversion	31
<i>In situ</i> activation–graphitization	Potassium citrate and iron citrate	Carbonized at 700–800 °C	HPGC-T	Energy storage, supercapacitor	34
Chemical activation–graphitization	PANI hydrogel	Carbonized at 400–900 °C	3D HPG	Energy storage, supercapacitor	7
Flash Joule heating	Graphene oxide	Heated at 3 000 K (~300 K min <sup>-1</sup> )	NP@rGO aerogel	—	35
Molten salt-assisted	ZIF-8 powder and NaCl	Heated at 950 °C	PM <sub>1</sub> /N-C <sub>Pores</sub>	Electrocatalytic	19

due to ionic confinement and enhanced heat transfer,<sup>19</sup> while ultrafast flash Joule heating (FJH) reaches over 3 000 K for below 1 s, producing graphitized carbons in kilogram-scale at only 2–3 kWh kg<sup>-1</sup>.<sup>31</sup>

**2.5.2. Scalability.** Hard-templating remains the least scalable technique because both the templating and template removal steps impose intrinsic throughput limitations.<sup>1,6,29,32</sup> Soft-templating routes, which base on amphiphilic micelles or block copolymers, provide better scalability, although their reproducibility can be influenced by precursor and micelle stability.<sup>10–12,24–26</sup> CVD provides excellent crystallinity but is still limited in reactor size.<sup>8,10–12</sup> MOF-derived carbons offer moderate scalability, but precursor costs interfere large-scale adoption.<sup>13,14,16–18,29</sup> Recent advances in molten-salt and FJH processes demonstrate the highest scalability potential, particularly for biomass-derived PGFs, since both molten salts and FJH processes enable high-volume, low-cost throughput.<sup>19,31</sup>

**2.5.3. Structural control.** Hard-templated PGFs exhibit the high pore precision, as the sacrificial template allows determined pore architectures.<sup>6</sup> Soft-templating generates uniform mesopores *via* micellar assemblies but provides less control over micropores.<sup>10–12,24–26</sup> CVD enables atomic-level crystalline control, although internal porosity is difficult to regulate without additional scaffolds.<sup>6–9</sup> MOF-derived PGFs offer well-defined microporous frameworks but frequently show collapses, resulting in heterogeneous porosity.<sup>16–18</sup> Molten-salt routes provide excellent micropore sculpting and dopant stabilization, as molten salt ions keep structural development and prevent collapse.<sup>19</sup> In contrast, FJH provides rapid

graphitization. However, the ultrafast heating (<1 s) leads to less predictable pore formation despite high crystallinity.<sup>31</sup>

## 2.6. Emerging PGF synthesis strategies and perspectives

Emerging inside-out activation methodologies (*e.g.*, K/Fe-mediated hierarchical graphitization) have produced materials with high surface area (>3 000 m<sup>2</sup> g<sup>-1</sup>) while maintaining conductivity.<sup>34</sup> Molten-salt-mediated graphitization has enabled the formation of single-atom-stabilized porous graphitic carbons, such as Ru-N<sub>4</sub> systems with high electrochemical performance.<sup>19</sup> Flash Joule heating (FJH) has enabled ultrafast (<1 s) graphitization of biomass and polymers, producing high-SSA carbons at a lower energy cost than conventional thermal routes.<sup>31,35</sup>

In general, despite the advantages, these methods also have various disadvantages that need to be addressed. For instance, hard-templated PGFs remain difficult to scale due to multi-step template removal, energy-intensive calcination, and the high cost and waste generation associated with etching agents.<sup>6,8</sup> CVD methods, though capable of producing highly crystalline sp<sup>2</sup> frameworks, are limited by low throughput, precursor inefficiency, and reactor retention time limitations, as emphasized in fluidized-bed graphene growth studies. Conversely, MOF/ZIF-derived graphitic carbons demonstrate promising scalability but face precursor heterogeneity and high-temperature requirements.<sup>9,13,16–18</sup> Emerging molten-salt and flash Joule heating routes offer increased scalability but are still challenged by batch size limitations, uniform heat distribution,

and trade-offs between graphitization and dopant retention.<sup>19,35</sup> These challenges of the technical constraints limit industrial implementation of PGFs.

It can be emphasized that although diverse PGF synthesis platforms, such as hard/soft templating, CVD, MOF/COF pyrolysis, molten-salt graphitization, flash Joule heating, have made significant progress, there is no generalized and standardized methodology achieving simultaneous scalability, high graphitization, precise pore control, and sustainable processing. Hard templates remain the most structurally deterministic but are energy- and waste-intensive.<sup>6,8</sup> Soft templates excel in scalability but struggle with high-temperature graphitization.<sup>11</sup> MOF-/ZIF-derived PGFs provide chemically rich frameworks but face precursor cost and structural heterogeneity issues.<sup>9,13</sup> Therefore, hybridized, multi-modal synthesis approaches are the most promising future direction.

Collectively, the template-directed assembly offers unmatched geometric precision, CVD offers crystallinity, pyrolysis provides chemical variability, and activation offers an ultrahigh surface area. Future synthetic paradigms will likely hybridize these modalities, for example, template-free salt activation with subsequent low-pressure CVD healing, to realize PGFs that optimize graphitic continuity with multiscale porosity while satisfying life-cycle sustainability metrics.

### 3. Structural characteristics

The formation of PGFs is typically validated by different essential characterization techniques, such as Raman and XRD spectroscopy for disorder or graphitic domain size ( $I_D/I_G$  ratios, D-band width),<sup>36,37</sup> pair distribution function (PDF) analysis for turbostratic stacking and crystallite size,<sup>14</sup> N<sub>2</sub> adsorption/desorption for BET surface areas or pore-size distribution in both crystalline and disordered carbonaceous frameworks,<sup>36</sup> TEM or HRTEM for direct imaging of graphitic fringes, and XPS for heteroatom configurations (N-pyridinic, N-graphitic, *etc.*). This toolbox was informed by recent structural-characterization review,<sup>14</sup> providing various useful characterization outputs and synthetic strategy.

#### 3.1. High surface area

The defining textural attribute of PGFs is their ability to sustain Brunauer–Emmett–Teller (BET) surface areas that rival, and in some cases exceed, those of conventional activated carbon, while retaining an electrically percolating sp<sup>2</sup> lattice. Recent examples underscore the effectiveness of synchronous activation–graphitization chemistry.<sup>7,38</sup> Singh *et al.* (2024) reported KOH/Fe-catalyzed carbothermic conversion of lignocellulosic precursors that produced nanoporous carbon–ceria composites with tunable SSA up to 1.997 m<sup>2</sup> g<sup>-1</sup> without compromising graphitic order.<sup>38</sup> Higher values can be achieved when chemical activation is coupled with rigid conjugated polymer templates. To *et al.* (2015) achieved 4.073 m<sup>2</sup> g<sup>-1</sup> in a 3D hierarchically porous graphitic (HPG) carbon prepared from a phytic-acid-cross-linked polyaniline molecular framework, demonstrating that graphitization can proceed at 800 °C provided that the

aromatic backbone is topologically locked prior to carbonization (Fig. 3A and B).<sup>7</sup> Such ultrahigh-area PGFs mitigate the classical tradeoff between capacitance and rate capability in electrochemical double-layer capacitors by maximizing the ion-accessible area without introducing insulating amorphous carbon.

#### 3.2. Tunable pore size

Beyond the magnitude, the distribution and connectivity of pores dictate the mass-transport phenomena. The carbonization of mixed-matrix precursors containing amorphous and crystalline ZIF-8 has emerged as a powerful route to achieve polymodal porosity. Hu *et al.* (2024) showed that the *in situ* dispersion of single Zn atoms within a carbon molecular-sieve membrane allows carbonization temperature (Fig. 3C) to dial the ultra-micro pore cutoff from 2.1 Å to 4 Å, enabling H<sub>2</sub>/CO<sub>2</sub> selectivity up to 130 and H<sub>2</sub>/CH<sub>4</sub> selectivity of 2.900. These values eclipse Robeson's upper bound for polymeric membranes (Fig. 3D and E).<sup>9</sup> Complementary Monte-Carlo simulations of Kr adsorption in slit pores corroborate that Ångström-level aperture control can be extracted from noble gas sorption isotherms, providing rapid metrology for the pore-size profiling of graphitic carbon.<sup>36</sup> Hierarchical design principles combine sacrificial hard templates (*e.g.*, MgO microspheres) for macroporosity with *in situ* catalytic activation to generate concentric micro- and mesopores, yielding surface-to-volume ratios that are optimized for both diffusion- and adsorption-limited applications.

#### 3.3. Graphitic domains

The continuity and size of the sp<sup>2</sup> domains govern charge transport, thermal stability, and chemical robustness. Quantitative Raman metrics, principally the  $I_D/I_G$  ratio and D-band full width at half-maximum, provide a proxy for the in-plane crystallite size ( $L_a$ ) *via* the Tuinstra–Koenig formalism. A comparative study of 20 nanoporous carbons demonstrated that smaller graphene-like domains (lower  $I_D/I_G$ ) correlated with enhanced supercapacitor capacitance, linking electronic disorder to ion-sieving efficiency.<sup>37</sup> In hierarchically porous Zn-embedded carbons, the progressive drop in  $I_D/I_G$  from 1.12 to 0.86 as carbonization temperature increased from 500 °C to 900 °C paralleled the emergence of a (002) reflection at 44°, confirming turbostratic stacking of graphitic layers.<sup>9</sup> The total -scattering pair-distribution-function analyses further revealed that the nanocrystalline domains extend 2–4 nm and are intergrown with amorphous regions. This mixed ordering reconciles high conductivity (>10 S cm<sup>-1</sup>) with the defect sites necessary for catalytic functionality.<sup>14</sup> Finally, edge-plane density, quantified *via* Kr adsorption differentials, has emerged as a critical descriptor for redox catalysis, offering a handle to balance basal-plane transport with edge-site reactivity in next-generation PGFs.<sup>39</sup>

#### 3.4. Trade-offs, structure–property gaps, and perspectives

While several studies claim simultaneous optimization of both properties, recent Raman-based disorder analyses reveal that



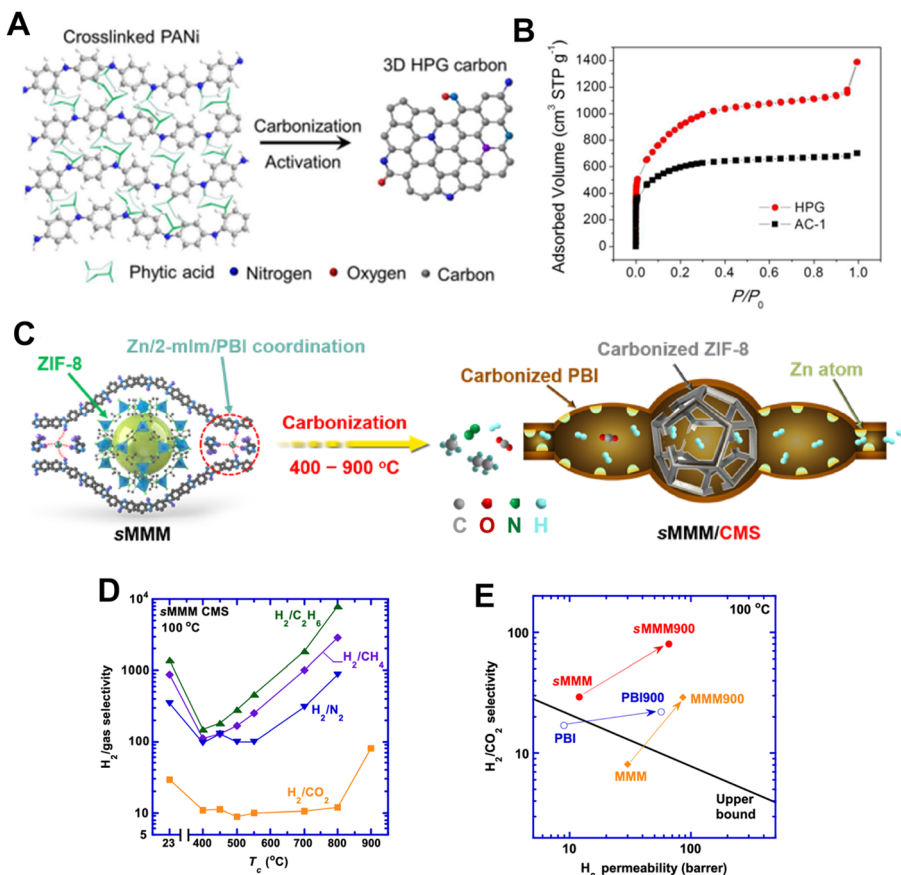


Fig. 3 (A) Transformation of phytic-acid-crosslinked PANi (left) into doped graphene-like carbon sheets.<sup>7</sup> (B) N<sub>2</sub> adsorption/desorption isotherm of HPG carbon, clearly showing a hierarchically porous structure.<sup>7</sup> Reuse permission from To *et al.* (2015)<sup>7</sup> by American Chemical Society. (C) Schematic illustration of the carbonization of a supramolecular mixed-matrix material (sMMM) to form CMS materials containing polymodal free volumes from 400 to 900 °C.<sup>9</sup> Reuse permission from Hu *et al.* (2024)<sup>9</sup> by Nature, under a Creative Commons Attribution 4.0 International License (<https://creativecommons.org/licenses/by/4.0/>). (D) H<sub>2</sub>/gas selectivity at 100 °C showcasing the flexible tunability of separation properties by varying carbonization temperature (T<sub>c</sub>).<sup>35</sup> Reuse permission from Xia *et al.* (2024)<sup>35</sup> by American Chemical Society, under a Creative Commons Attribution 4.0 International License (<https://creativecommons.org/licenses/by/4.0/>). (E) Superior H<sub>2</sub>/CO<sub>2</sub> separation properties of sMMM900 (E).<sup>9</sup> Reuse permission from Hu *et al.* (2024)<sup>9</sup> by Nature, under a Creative Commons Attribution 4.0 International License (<https://creativecommons.org/licenses/by/4.0/>).

increased ultra-micro porosity often correlates with reduced sp<sup>2</sup> domain continuity, leading to higher  $I_D/I_G$  ratios and lower electronic mobility.<sup>37,40</sup> Conversely, highly crystalline PGFs, such as those obtained *via* catalytic graphitization, show improved conductivity but present pore collapse or loss of ultra-micro pores needed for adsorption and ion transport.<sup>7,14</sup> It can be emphasized that resolving this issue remains a challenge, which may not be suitable across systems.

The inconsistencies in pore-size characterization, defect quantification, and graphitization indexing differ across measurement techniques and can lead to inconsistent interpretations across studies. For example, Kr adsorption and GCMC simulations provide Å-level accuracy for micropore distributions, but they are not yet standard in non-nuclear graphite research.<sup>36</sup> Similarly, Raman  $I_D/I_G$  ratios vary with laser wavelength and cannot always distinguish between edge defects and in-plane vacancies. PDF analysis, while powerful, remains low capability of utilization due to instrumentation challenges.<sup>14</sup>

Raman spectroscopy clearly correlates disorder with pseudocapacitive enhancement in nanoporous carbons,<sup>37</sup> but this conflict with the systems where improved crystallinity provides superior electron transport.<sup>7</sup> Similarly, PDF analysis has revealed that many PGFs contain heterogeneous mixtures of amorphous and nanocrystalline domains, complicating predictions of performance based on XRD alone.<sup>14</sup> Additionally, Kr adsorption has recently emerged as a sensitive probe for edge-plane density. However, few studies employ this technique despite its utility in correlating defect sites with catalytic performance.<sup>36</sup> These studies imply the gaps in comparison across PGF systems.

Although structural analysis tools (N<sub>2</sub> sorption, Raman, XRD, PDF, Kr adsorption) have become highly useful, there is no unified quantitative framework linking hierarchical porosity, graphitic domain size, edge-plane density, and electronic structure. For example, PDF analysis reveals coexistence of amorphous and nanocrystalline carbon regions,<sup>14</sup> Raman  $I_D/I_G$  correlations vary by excitation wavelength,<sup>37</sup> and Kr adsorption

probes edge-plane density<sup>36</sup> but it is hardly used outside nuclear graphite research. Standardized measurement is essential for future PGF design.

## 4. Properties

### 4.1. Electrical conductivity

PGFs inherit the delocalized  $\pi$ -electron network of graphite, yet their conductivity is ultimately dictated by the continuity of  $sp^2$  domains and the density of charge-scattering defects.<sup>40</sup> Four-probe measurements on a wood-waste-derived, N-doped multiporous carbon (N-GMPC) recently reached  $9.4 \text{ S cm}^{-1}$  while

preserving a BET area of  $1638 \text{ m}^2 \text{ g}^{-1}$ . Density-functional calculations attributed this synergy to pyridinic-N-induced band broadening, which lowered the carrier effective mass (Fig. 4A).<sup>41</sup> Comparable conductivities ( $>10 \text{ S cm}^{-1}$ ) were reported for hierarchical porous graphitic carbons synthesized by inside-out K/Fe activation, where atomically dispersed Fe catalyzed lattice ordering during pore generation.<sup>34</sup> These studies overcome the classical porosity-conductivity tradeoff by demonstrating that controlled graphitization and heteroatom modulation can furnish bicontinuous electronic and ionic highways, which are prerequisites for high-rate electrochemical energy storage.

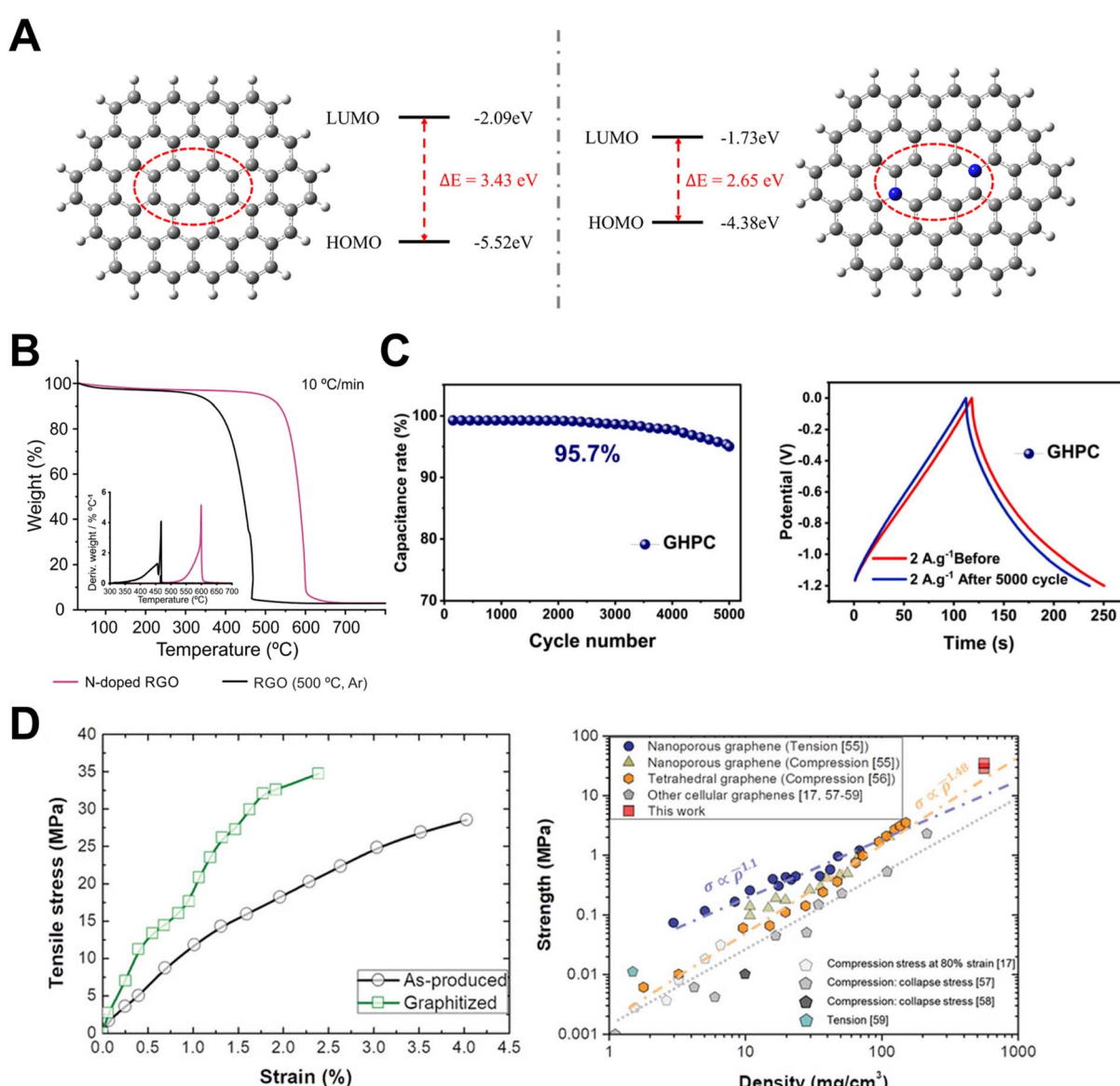


Fig. 4 (A) Density functional calculations of energy gaps in pyridinic N-doped and undoped carbon materials.<sup>41</sup> Reuse permission from Wang *et al.* (2025)<sup>41</sup> by The Royal Society of Chemistry, under a Creative Commons Attribution 4.0 International License (<https://creativecommons.org/licenses/by/4.0/>). (B) TGA curves of the RGO and N-doped RGO.<sup>42</sup> Reuse permission from Martincic *et al.* (2024)<sup>42</sup> by MDPI, under a Creative Commons Attribution 4.0 International License (<https://creativecommons.org/licenses/by/4.0/>). (C) Cyclic stability of the GHPC electrode.<sup>30</sup> Reuse permission from Guye *et al.* (2025)<sup>30</sup> by Elsevier. (D) Stress–strain curves and strength versus density of porous graphitic carbon materials.<sup>44</sup> Reuse permission from Polyakova *et al.* (2023)<sup>44</sup> by MDPI, under a Creative Commons Attribution 4.0 International License (<https://creativecommons.org/licenses/by/4.0/>).

#### 4.2. Thermal stability

The strong in-plane  $\sigma$ -bonds of graphitic carbon endow PGFs with exceptional resistance to thermally driven lattice degradation. Thermogravimetric analysis (TGA) of multilayer graphene and CNT analogs showed an oxidation onset ( $T_{\text{onset}}$ ) in air above 500 °C, rising toward 650 °C as the degree of graphitization increased (Fig. 4B).<sup>42</sup> Hierarchical porous graphitic carbons fabricated by metallothermic reduction maintained 95% of initial capacitance when cycled at 150 °C in ionic-liquid electrolytes, confirming functional stability under harsh thermal loads.<sup>43</sup> Potassium-catalyzed graphitization further lowers the energy cost of producing such heat-resilient carbons, enabling crystallite development below 1 000 °C without sacrificing porosity. This is a key sustainability advancement in large-scale syntheses.<sup>32</sup>

#### 4.3. Chemical stability

Chemical inertness is critical when the interface with strongly acidic, alkaline, or oxidative. Self-heteroatom-doped porous carbons derived from *Mikania micrantha* retained >90% capacitance after 10 000 cycles in 1 M H<sub>2</sub>SO<sub>4</sub>, highlighting the role of graphitic domains in suppressing carbon corrosion.<sup>45</sup> In alkaline media, bio-templated graphitic frameworks sustained 95.7% capacity over 5 000 cycles at 2 A g<sup>-1</sup>, with post-mortem X-ray photoelectron spectroscopy revealing minimal surface oxidation, again underscoring the chemical passivation imparted by extended sp<sup>2</sup> conjugation (Fig. 4C).<sup>30</sup> Molecular simulations of hydroxyl radical attack on graphitic edges indicated activation barriers of >1.5 eV, corroborating the experimental durability trends and suggesting that selective edge functionalization, rather than basal-plane degradation, governs long-term stability in electrochemical reactors.<sup>46</sup>

#### 4.4. Mechanical strength

Although porosity usually compromises the mechanical integrity, PGFs leverage the high intrinsic modulus of graphene to achieve remarkable strength-to-weight ratios. Molecular-dynamics simulations predicted compressive strengths of up to 2 GPa at 70% strain for multilayer graphene networks, facilitated by out-of-plane buckling and interlayer friction that dissipate energy without catastrophic failure (Fig. 4D).<sup>44</sup> Experimentally, MOF-derived porous graphitic carbon reinforced with residual metal nanonodes exhibited a Young's modulus of 34.8 MPa and recovered 95% of the original height after 1 000 compression cycles, demonstrating the super-elastic behavior desirable for flexible devices.<sup>47</sup> These findings suggest that the strategic incorporation of graphitic struts and hierarchical cell walls can reconcile high surface areas with load-bearing capacities, thereby opening avenues for the development of structural energy-storage composites and thermally stable insulation foams.

Mechanical/thermal stabilities and conductivity are mutually dependent. Therefore, it is difficult to optimize simultaneously. Insights from examples, such as conductive N-doped carbons (>9 S cm<sup>-1</sup>)<sup>41</sup> and solid nanocellular graphene

architectures,<sup>47</sup> underscore the balance between defect density, graphitic order, and porosity. The challenge is that multi-property optimization (porosity, conductivity, mechanical stability) remains one of the field's most significant unsolved aspects. Collectively, the unique combination of high electrical conductivity, thermal/chemical robustness, and tunable mechanical resilience makes PGFs a versatile platform for next-generation electrochemical, catalytic, and structural applications.

### 5. Applications

#### 5.1. Energy storage

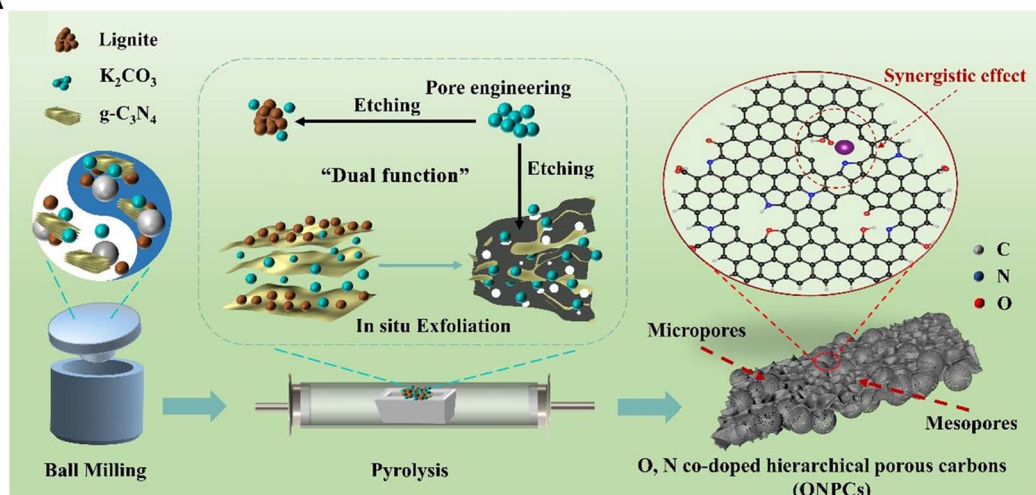
The integration of high surface area, and hierarchical porosity with extended sp<sup>2</sup> conjugation continues to elevate the performance of PGFs in electrochemical energy storage.<sup>40</sup> For example, machine-learning (ML)-guided optimization of an O,N co-doped hierarchical PGF (ONPC-900) recently delivered a gravimetric capacitance of 440 F g<sup>-1</sup> at 0.5 A g<sup>-1</sup> and preserved 92% of that value after 10 000 cycles (Fig. 5A and B). Density-functional calculations ascribed the performance boost to synergistic ion adsorption at the pyrrolic-N and -COOH sites embedded in the graphitic walls, demonstrating the synergistic contribution of O,N surface functionalities to ion-accessible adsorption sites and conductivity.<sup>33</sup> Similarly, high-surface-area hierarchical PGFs derived from conjugated polymer frameworks, with high SSA (approximately 4073 m<sup>2</sup> g<sup>-1</sup>) deliver rapid charge-discharge behavior without the diffusion limitations typically observed in activated carbons.<sup>7</sup> Complementary "inside-out" K/Fe activation-graphitization has demonstrated that conductive graphitic backbones can coexist with 3 000 m<sup>2</sup> g<sup>-1</sup> of accessible surface, yielding 322 F g<sup>-1</sup> and 101% capacitance retention over 15 000 cycles in symmetric supercapacitors.<sup>34</sup> These studies collectively show that heteroatom chemistry and catalytic graphitization can reconcile the historic trade-off between porosity and electronic conductivity, enabling PGF electrodes that operate at >10 A g<sup>-1</sup> without severe IR drop, which attributes now being translated into Zn-ion hybrid and Li-S full-cell architectures. It demonstrates PGFs as one of the few materials classes that can provide both rate and stability requirements for next-generation supercapacitors.<sup>34,48</sup>

#### 5.2. Catalysis

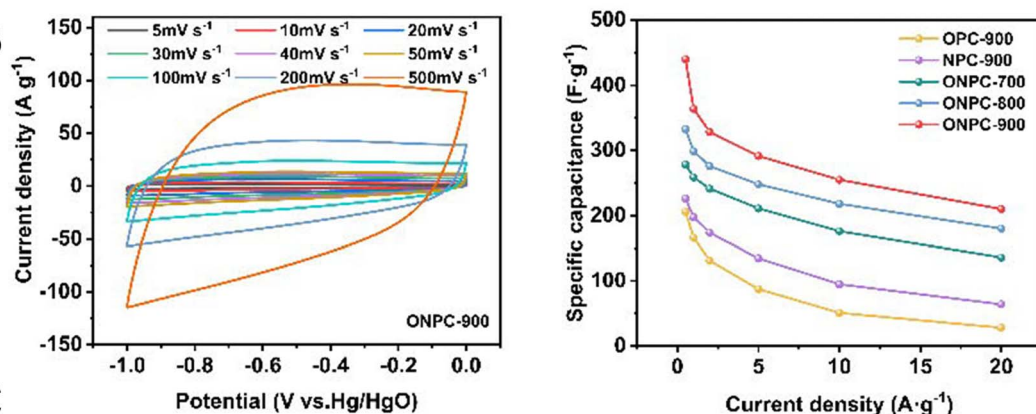
In electrocatalysis, PGFs provide tunable defect topologies and high electronic mobility that effectively stabilize atomically dispersed active sites.<sup>13</sup> The catalytic performance of PGFs depends on the interplay between the edge-plane defects (active sites) and graphitic continuity (electron transport). A pore-edge graphitic-nitride framework prepared via SiO<sub>2</sub>-protected templating exhibits a half-wave potential of 0.842 V for the oxygen-reduction reaction and sustains 779 mA h g<sub>Zn</sub><sup>-1</sup> in liquid Zn-air batteries, outperforming numerous metal- N- C benchmarks. The authors attributed this activity to the vacancy-enriched N at the pore rims coupled with hierarchical ion pathways.<sup>49</sup> Extending this paradigm, Ru-N<sub>4</sub> single atoms anchored on Ni-MOF-derived PGF achieve overpotentials of only 54 mV (HER)



A



B



C

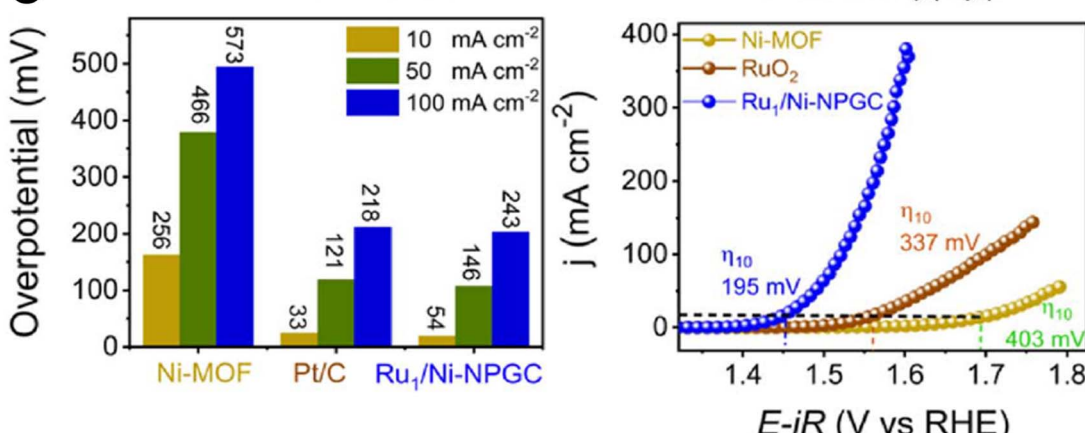


Fig. 5 (A) Schematic of synergistically fabricated ONPC materials.<sup>33</sup> (B) CV plots of ONPC-900 measured at various scans (5–500 mV s<sup>-1</sup>) and SC comparison of ONPC materials measured at different current densities.<sup>33</sup> Reuse permission from Liu et al. (2025)<sup>33</sup> by OAE Publishing Inc., under a Creative Commons Attribution 4.0 International License (<https://creativecommons.org/licenses/by/4.0/>). (C) HER performance of Ru<sub>1</sub>/Ni-NPGC catalysts and iR-corrected OER polarization curves (scan rate 1 mV s<sup>-1</sup>).<sup>13</sup> Reuse permission from Mishra et al. (2025)<sup>13</sup> by The Royal Society of Chemistry.

and 195 mV (OER) at 10 mA cm<sup>-2</sup> (Fig. 5C) across the full pH window. They are competitive with noble metal benchmarks.<sup>49</sup> This observation underscores the mechanism by which atomically dispersed metals are stabilized by the strong metal-support interactions within graphitic lattices.<sup>13</sup> These results highlight the potential of PGFs as tunable corrosion-resistant

scaffolds for both electrocatalytic redox reactions and thermo-catalytic transformations.

### 5.3. Gas storage and separation

The ultra-micro porous regime (<0.7 nm) accessible in PGFs affords binding enthalpies well-matched to H<sub>2</sub> and CO<sub>2</sub>



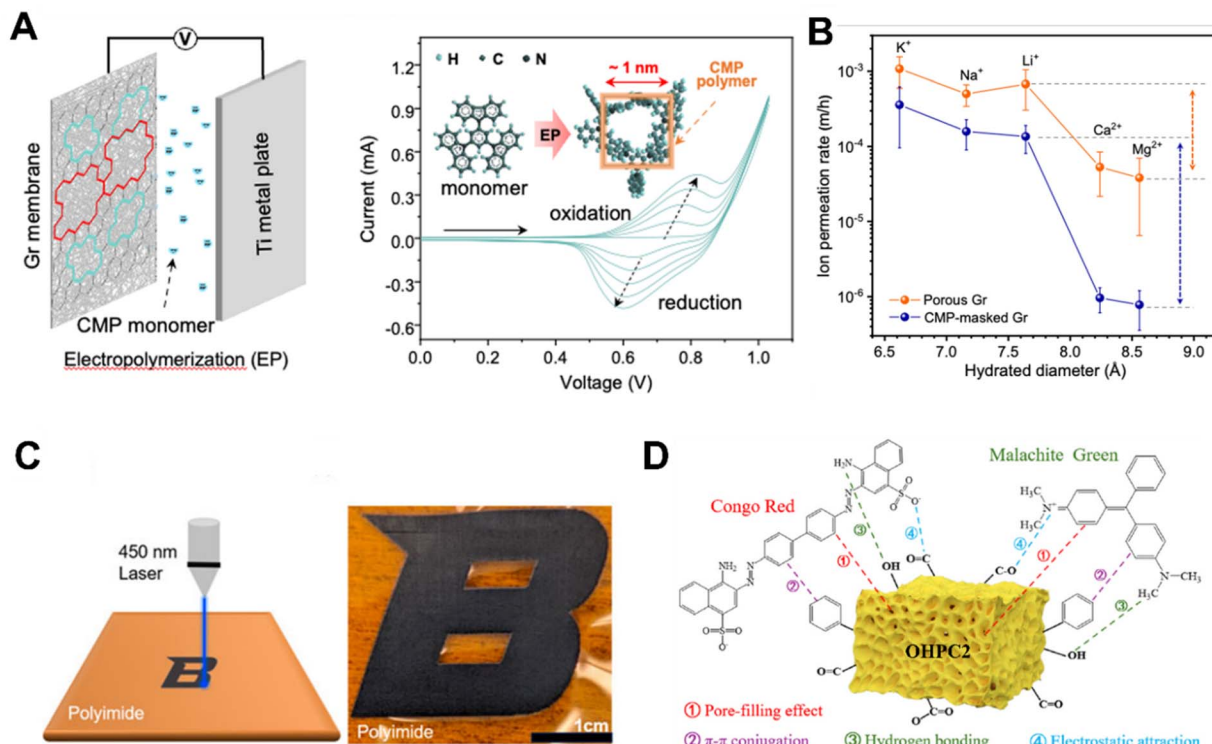


**Fig. 6** (A) Schematic of the electrochemical repair device and cyclic voltammetry profiles of the electrochemical repair process.<sup>51</sup> (B) Ion–ion separation performance of CMP-masked porous graphene membranes.<sup>51</sup> Reuse permission from Zhou *et al.* (2024)<sup>51</sup> by Springer Nature, under a Creative Commons Attribution 4.0 International License (<https://creativecommons.org/licenses/by/4.0/>). (C) Schematic of LIG fabrication and optical image of the patterned LIG.<sup>52</sup> Reuse permission from Francis *et al.* (2024)<sup>52</sup> by Frontiers Media S.A., under a Creative Commons Attribution 4.0 International License (<https://creativecommons.org/licenses/by/4.0/>). (D) Schematic of the possible mechanisms of CR and MG adsorption by OHPC2.<sup>53</sup> Reuse permission from Zhang *et al.* (2025)<sup>53</sup> by Elsevier.

physisorption. A review of adsorption-based H<sub>2</sub> storage reports that graphitic carbons with pore volumes enriched below 0.6 nm routinely surpass 6 wt% uptake at 77 K and 100 bar, with sp<sup>2</sup> content emerging as a key predictor of isosteric heat.<sup>50</sup> For separations, defect-engineered monolayer graphene repaired by a 10 nm conjugated microporous polymer masks non-selective pores and achieves Li<sup>+</sup>/Mg<sup>2+</sup> selectivity of 300 alongside high flux, demonstrating Å-scale sieving combined with mechanical integrity (Fig. 6A and B).<sup>51</sup> Recent breakthroughs in Å-precision porosity illustrate the growing potential of PGFs in gas purification. Carbon molecular sieves incorporating single Zn atoms and tightly confined ultra-micro pores demonstrate H<sub>2</sub>/CO<sub>2</sub> selectivity values reaching 130, and H<sub>2</sub>/CH<sub>4</sub> selectivity as high as 2900. These performance metrics that exceed the Robeson bounds for polymer membranes.<sup>9</sup> These results come from finely-tuned pore in the 2.1–4.0 Å range. They are regulated by carbonization temperature and metal-assisted carbon rearrangements. The graphitic backbone provides both mechanical stability, enabling PGF-derived membranes to operate under rough thermal and pressure that challenge traditional polymer systems. These advances have enabled PGF membranes to meet the simultaneous demands of permeability, selectivity, and stability required for hydrogen purification and post-combustion CO<sub>2</sub> capture.

#### 5.4. Sensors

Porous graphitic architectures also underpin next-generation chemiresistive platforms. Laser-induced graphene (LIG) fabricated on polyimide *via* 450 nm photothermal writing yields a defect-rich (Fig. 6C), 3D graphitic foam whose resistance changes by up to 5% in response to sub-ppm volatile organic compounds at room temperature. The porous morphology and nanometer-scale crystallites provided abundant adsorption sites while maintaining flexibility over 100 bending cycles.<sup>52</sup> The low-cost and patternable nature of LIG demonstrate how PGF principles can be leveraged for scalable environmental monitoring and wearable analytics.

#### 5.5. Adsorption

Finally, the combination of hierarchical porosity and π-rich basal planes endows PGFs with exceptional sorptive capacities for aqueous contaminants. An oxidized hierarchical porous carbon featuring vesicle-like ultrathin graphitic walls exhibits Langmuir capacities of 2.729 mg g<sup>-1</sup> for Congo red and 1.697 mg g<sup>-1</sup> for malachite green, with regeneration efficiencies above 90% over five cycles. These capacities exceed those of typical activated carbons, due to the combined mechanistic contributions of π-π stacking, pore filling, surface hydrogen bonding, and favorable electrostatic interactions within



Table 2 Comparative performance metrics of PGFs in various applications

Applications	Representative PGF	Key structural features	Performance metrics	Ref.
Supercapacitors	ONPC-900	Hierarchical micro-mesoporosity; O,N co-doping	440 F g <sup>-1</sup> at 0.5 A g <sup>-1</sup> ; 92% retention after 10 000 cycles	33
Supercapacitors	HPG carbon	Crosslinked PANi-derived 3D conjugated framework	BET ~4073 m <sup>2</sup> g <sup>-1</sup> ; high-rate stability	7
Electrocatalysis (HER/OER)	Ru-N <sub>4</sub> /Ni-MOF-PGF	Atomically dispersed Ru-N <sub>4</sub> sites; graphitic channels	54 mV (HER) and 195 mV (OER) at 10 mA cm <sup>-2</sup>	13
ORR catalysis	Pore-edge graphitic nitride PGF	Vacancy-enriched N, hierarchical channels	Half-wave potential: 0.842 V; Zn-air discharge: 779 mA h g <sub>Zn</sub> <sup>-1</sup>	49
H <sub>2</sub> /CO <sub>2</sub> separation	Zn-embedded CMS (PGF-like)	Å-precision ultra-micro pores <i>via</i> controlled carbonization	Selectivity: H <sub>2</sub> /CO <sub>2</sub> = 130; H <sub>2</sub> /CH <sub>4</sub> = 2900	9
Gas adsorption (pollutants)	OHPC2	Vesicle-like ultrathin graphitic walls	$q_{\max} = 2729 \text{ mg g}^{-1}$ (Congo red); 1697 mg g <sup>-1</sup> (MG)	53
Mechanical stability	MOF-derived graphitic nanocellular carbon	Interconnected graphitic struts; metal nanonodes	Young's modulus: 34.8 MPa; 95% height recovery after 1000 cycles	47
Thermal stability	Hierarchical graphitic carbon	High graphitization index	Capacitance stability at 150 °C over 10 000 cycles	43

ultrathin graphene-like domains (Fig. 6D).<sup>53</sup> This advantageous performance, achieved without metal additives, positions PGFs as sustainable adsorbents for dye-rich industrial effluents and emerging micropollutants.

### 5.6. Practical limitations and perspectives

Supercapacitor studies using high surface-area PGFs often demonstrate excellent cycling stability of electrodes at small laboratory scale but do not report volumetric performance, electrolyte compatibility, or mechanical integration, which factors crucial for device-level use.<sup>34,48</sup> Although single-atom PGF electrocatalysts such as RuN<sub>4</sub> show excellent HER/OER kinetics,<sup>13</sup> long-term tolerance and large-scale electrode integration remain elusive. Besides, their stability under industrial electrolyte impurities, agglomeration resistance, and mass transport under realistic flow conditions are not yet adequately explored.<sup>13</sup> Membrane applications (H<sub>2</sub>/CO<sub>2</sub> separation) using ultra-micro porous PGFs<sup>9</sup> shows superior selectivity but meet the challenges in mechanical stability, defects control, and trade-offs between permeability and long-term changes in selectivity. These issues limit of the technological applications of PGF-based devices.

For energy storage, O,N-co-doped hierarchical PGFs<sup>33</sup> achieve high gravimetric capacitance but lack data on volumetric performance, electrode densification, and industrial electrolyte compatibility. In catalysis, Ru-N<sub>4</sub> PGFs<sup>30</sup> show outstanding HER/OER activity, however, long-term stability against metal migration remains less understood. For gas separation, single-atom Zn-embedded molecular sieve carbons<sup>9</sup> demonstrate remarkable H<sub>2</sub>/CO<sub>2</sub> selectivity, but still face mechanical limitations in membrane-scale fabrication. For sensing, laser-induced graphitic foams<sup>52</sup> show high sensitivity but require improvements in signal and environmental stabilities. It can be clearly stated that scaling from gram-scale performances to

device-level deployment is the most critical next step. These cases illustrate method limitations that remain unresolved.

Collectively, these application domains show that rational control over the pore architecture, graphitic order, and heteroatom chemistry transforms PGFs from structural curiosities into multifunctional workhorses spanning energy, environment, and sensing technologies (Table 2).

## 6. Outlook and future perspectives

### 6.1. Advanced synthesis techniques

The next decade could shift from slow equilibrium-controlled pyrolysis to kinetically driven data-assisted manufacturing routes for PGFs. Ultrafast flash-Joule heating (FJH) already converts diverse solid wastes or graphene-oxide aerogels into milligram-to-kilogram batches of 3D "flash graphene" within <1 s, reaching peak temperatures >3 000 K and specific surface areas above 1 000 m<sup>2</sup> g<sup>-1</sup> while consuming only 2–3 kWh kg<sup>-1</sup> of the product.<sup>35,54</sup> Scientific machine-learning models trained on FJH process variables can predict graphene yields with  $R^2 \approx 0.8$ , functioning as closed-loop reactors that optimize porosity and graphitic order in real time.<sup>54</sup> In parallel, molten-salt media such as LiCl/KCl or ZnCl<sub>2</sub> not only act as high-temperature solvents but also template nanoscale voids and scavenge heteroatoms. A recent molten-salt-assisted route produced Ru-single-atom/porous-N-graphitic carbons with metal loadings of up to 4.3 wt% and turnover frequencies rivaling those of Pt for water electrolysis.<sup>19</sup> Additive manufacturing closes this gap in geometric properties. Inverse-designed electrodes fabricated by direct-ink-writing of graphene aerogel lattices lowered power losses in flow reactors by 16% relative to homogeneous porosity controls, proving that micron-resolved porosity gradients can be printed and pyrolyzed without sacrificing electrical consecutiveness.<sup>55</sup> Collectively, the convergence of FJH, molten-salt



chemistry, and 3-D printing promises kilogram-scale production of architected PGFs with programmable pore topology/crystallinity.

## 6.2. Enhanced functionalization

Beyond skeleton engineering, the future performance of devices will be based on precise electronic and chemical tailoring of the graphitic backbone. Single-atom metallurgy is a rapidly developing field of research. For instance, Ru-N<sub>4</sub> moieties stabilized on Ni-MOF-derived PGFs drive pH-universal overall water splitting at 10 mA cm<sup>-2</sup> with overpotentials of only 54 mV (HER) and 195 mV (OER), benefiting from strong metal-support interactions within nitrogen-coordinated graphene cavities.<sup>13</sup> Additionally, post-synthetic covalent chemistry offers a complementary avenue. Advances in diazonium, click, and Pictet-Spengler reactions have enabled nanometer-resolved grafting of redox mediators or ionic anchors without collapsing the pore network, as exemplified by a one-pot Pictet-Spengler polymerization that installed proton-conducting benzimidazole rings throughout a mesoporous graphitic scaffold.<sup>56</sup> In addition, edge-selective ball-milling and plasma routes deliver kilogram-scale heteroatom doping with controllable N, P, or S speciation, as summarized in a study on sp<sup>2</sup>-carbon functionalization.<sup>57</sup> A promising trend is the development of a toolbox that couples atomic precision with macroscopic throughput, allowing catalytic, sensing, or sorptive sites to be defined independently of bulk conductivity.

## 6.3. Emerging applications

The structural and chemical versatility unlocked above provides a catalytic application space that extends well beyond classical electrochemistry. In electromagnetic-interference (EMI) shielding, hierarchical CNT/graphitic-carbon foams with engineered pore/graphite synergies already deliver >80 dB X-band attenuation at thicknesses of only 160 µm, an absorption-dominated mechanism that is attractive for lightweight aerospace electronics.<sup>58</sup> Gas-hydrate energy storage has also been proposed. Ultralight graphene aerogels act as fixed beds that nucleate methane hydrates inside 50–250 µm pores, raising volumetric storage capacity to 146 V V<sup>-1</sup> and mitigating expansion stresses that plague conventional pellets.<sup>59</sup> Biomedical technology is another mechanically resilient hybrid aerogel composed of dual-scale fibers and graphitic nanoflakes that supports rapid tissue ingrowth and neovascularization, while retaining superelastic recovery (1.8 s) under compressive loads, opening prospects for minimally invasive soft-tissue scaffolds and bioelectronic interfaces.<sup>60</sup> Finally, architected PGF electrodes, printed by inverse design, support electrochemical flow reactors and redox-flow batteries with reduced pumping energy and enhanced kinetics, illustrating the emerging role of digital manufacturing in translating pore-scale insights into device-level efficiency gains.<sup>55</sup>

## 6.4. Perspectives

PGFs have progressed from conceptual hybrids to a coherent material family whose synthesis–structure–property relationships can now be articulated with increasing precision.

Integrative routes that couple chemical activation with catalytic graphitization reconcile the long-standing porosity–conductivity trade-off, as exemplified by inside-out K/Fe strategies that deliver >300 F g<sup>-1</sup> capacitance alongside 10 S cm<sup>-1</sup> conductivity.<sup>34</sup> Parallel molten-salt chemistries embed transient ionic media to template subnanometer voids and stabilize heteroatom-rich edge planes, yielding surface areas above 2500 m<sup>2</sup> g<sup>-1</sup> while endowing catalytic functionality.<sup>61</sup> These advances confirm that hierarchical porosity, extended sp<sup>2</sup> conjugation, and site-specific heteroatom doping are not mutually exclusive. Instead, they can be co-engineered to unlock superior electrochemical, catalytic, and adsorptive performances. Scalability and sustainability, which are historical bottlenecks for designer carbons, were addressed using equilibrium manufacturing paradigms. Flash-Joule heating now converts biomass or polymer waste into kilogram-scale flash graphene within seconds, cutting energy demand to <5 kWh kg<sup>-1</sup> and reducing life-cycle CO<sub>2</sub> emissions by approximately 86% relative to conventional graphitization.<sup>31</sup> When integrated with automated control and data-driven process optimization, such ultrafast routes promise real-time tuning of pore topology and crystallinity, whereas molten-salt and additive-manufacturing techniques offer complementary pathways toward complex, application-specific architectures. Therefore, hybrid synthesis strategies (e.g., molten-salt + CVD healing; FJH + activation) represent the most promising forward-looking path. Besides, real-time process control (AI/ML-guided synthesis, *in situ* monitoring) will soon redefine PGF reproducibility and scalability.<sup>54,62</sup> Digital manufacturing and topology-optimized design will also unlock specific applications of PGFs for flow reactors, membranes, and energy devices.<sup>55</sup> In addition, sustainable and circular-carbon PGFs prepared from biomass or waste streams<sup>31,63,64</sup> will be increasingly essential. Collectively, these developments represent a potential route from laboratory gram-scale performances to the industrial production of architected PGFs.

The functional breadth of the PGFs has expanded. Nitrogen-doped, bio-derived frameworks already rival state-of-the-art activated carbons in supercapacitors while leveraging agricultural waste streams.<sup>63–65</sup> Absorption-dominated electromagnetic-interference shields achieve 80 dB effectiveness at ultralow areal densities, underscoring the utility of hierarchical graphitic foams in lightweight electronics.<sup>66</sup> However, opportunities remain unexplored, such as Ångström-resolved membranes for ion-sieving, biocompatible aerogels for regenerative medicine, and redox-mediated flow electrodes for large-scale energy storage. These benefits are attributed to the unique confluence of conductivity, stability, and tunable porosity intrinsic to PGFs. Realizing these prospects requires standardized metrology for pore/defect quantification, spectroscopy to map coupled ion-electron transport, and multiscale modeling frameworks that bridge atomistic chemistry with device-level performance.

## 7. Conclusions

In summary, the synthesis, functionalization, and deployment of PGFs are co-developing toward a future in which atomic-to-



device integration is common. Achieving this vision requires high-throughput, energy-saving fabrication with predictive modeling and application-specific surface chemistry, which is an interdisciplinary challenge that positions PGFs at the center of sustainable manufacturing, advanced catalysis, and next-generation multifunctional materials. The rapid development of advanced synthesis, precision functionalization, and emerging application spaces has made PGFs a promising option for next-generation carbon materials. Integration of sustainable manufacturing with atom-to-device design principles can be an effective strategy for developing multifunctional architectures to mitigate the challenges in clean energy, environmental remediation, and high-frequency electronics.

## Author contributions

Conceptualization, resources, writing, review, and editing: Minh Kim Nguyen, Ha Huu Do, Nguyen Tien Tran, and Young-Chul Lee.

## Conflicts of interest

The authors declare no conflicts of interest.

## Data availability

No primary research results, software or code have been included and no new data were generated or analysed as part of this review.

## Acknowledgements

The Basic Science Research Capacity Enhancement Project was funded through a grant from the Korea Basic Science Institute (National Research Facilities and Equipment Center), funded by the Ministry of Education of the Republic of Korea (2019R1A6C1010016).

## References

1. Devendran and A. Nagai, Recent advancements in 3D porous graphene-based electrode materials for electrochemical energy storage applications, *Mater. Adv.*, 2023, **4**, 2524–2543, DOI: [10.1039/D3MA00022B](https://doi.org/10.1039/D3MA00022B).
2. X. Li, H. Wang, H. Chen, Q. Zheng, Q. Zhang, H. Mao, Y. Liu, S. Cai, B. Sun, C. Dun, M. P. Gordon, H. Zheng, J. A. Reimer, J. J. Urban, J. Ciston, T. Tan, E. M. Chan, J. Zhang and Y. Liu, Dynamic Covalent Synthesis of Crystalline Porous Graphitic Frameworks, *Chem.*, 2020, **6**, 933–944, DOI: [10.1016/j.chempr.2020.01.011](https://doi.org/10.1016/j.chempr.2020.01.011).
3. C. Zhao, J. Yan, Z. Ma, Y. Zhang, T. Hu and H. Zhang, Recent advances in conjugated ladder-type porous polymer networks for rechargeable batteries, *Chem. Synth.*, 2025, **5**, 32, DOI: [10.20517/cs.2024.14](https://doi.org/10.20517/cs.2024.14).
4. B. Mishra, S. Biswal and B. P. Tripathi, Spinel Nickel Ferrite on Metal–Organic Framework-Derived Porous Carbon as a Robust Faradaic Electrode for Enhanced Flow Capacitive
5. H. Oka, N. Setoyama and S. Matsuhara, Gas adsorption analysis for quantifying the edge sites of graphite, *Carbon*, 2024, **230**, 119664, DOI: [10.1016/j.carbon.2024.119664](https://doi.org/10.1016/j.carbon.2024.119664).
6. E. Doustkhah, A. Kotb, S. Tafazoli, T. Balkan, S. Kaya, D. A. H. Hanaor and M. H. N. Assadi, Templated Synthesis of Exfoliated Porous Carbon with Dominant Graphitic Nitrogen, *ACS Mater. Au*, 2023, **3**, 231–241, DOI: [10.1021/acsmaterialsau.2c00074](https://doi.org/10.1021/acsmaterialsau.2c00074).
7. J. W. F. To, Z. Chen, H. Yao, J. He, K. Kim, H.-H. Chou, L. Pan, J. Wilcox, Y. Cui and Z. Bao, Ultrahigh Surface Area Three-Dimensional Porous Graphitic Carbon from Conjugated Polymeric Molecular Framework, *ACS Cent. Sci.*, 2015, **1**, 68–76, DOI: [10.1021/acscentsci.5b00149](https://doi.org/10.1021/acscentsci.5b00149).
8. X. Zhu, J. Ye, Y. Lu and X. Jia, 3D Graphene Nanostructure Composed of Porous Carbon Sheets and Interconnected Nanocages for High-Performance Lithium-Ion Battery Anodes and Lithium–Sulfur Batteries, *ACS Sustainable Chem. Eng.*, 2019, **7**, 11241–11249, DOI: [10.1021/acssuschemeng.9b00564](https://doi.org/10.1021/acssuschemeng.9b00564).
9. L. Hu, W.-I. Lee, S. Roy, A. Subramanian, K. Kisslinger, L. Zhu, S. Fan, S. Hwang, V. T. Bui, T. Tran, G. Zhang, Y. Ding, P. M. Ajayan, C.-Y. Nam and H. Lin, Hierarchically porous and single Zn atom-embedded carbon molecular sieves for H<sub>2</sub> separations, *Nat. Commun.*, 2024, **15**, 5688, DOI: [10.1038/s41467-024-49961-z](https://doi.org/10.1038/s41467-024-49961-z).
10. A. Ahmed, P. John, M. H. Nawaz, A. Hayat and M. Nasir, Zinc-Doped Mesoporous Graphitic Carbon Nitride for Colorimetric Detection of Hydrogen Peroxide, *ACS Appl. Nano Mater.*, 2019, **2**, 5156–5168, DOI: [10.1021/acsanm.9b01036](https://doi.org/10.1021/acsanm.9b01036).
11. Z. Wei, Z. Yanfei and W. Jiao, Mesoporous carbon materials: synthesis methods, properties, and advanced applications, *Front. Mater.*, 2025, **12**, 1548671.
12. S. Mehdipour-Ataei and E. Aram, Mesoporous Carbon-Based Materials: A Review of Synthesis, Modification, and Applications, *Catalysts*, 2023, **13**, 2, DOI: [10.3390/catal13010002](https://doi.org/10.3390/catal13010002).
13. B. Mishra, S. Biswal and B. P. Tripathi, Engineering Ru–N4 single atom catalysts on Ni-MOF-derived porous graphitic carbon for pH universal water electrolysis, *J. Mater. Chem. A*, 2025, **13**, 6792–6803, DOI: [10.1039/D4TA08969C](https://doi.org/10.1039/D4TA08969C).
14. I. Romero-Muñiz, E. Loukopoulos, Y. Xiong, F. Zamora and A. E. Platero-Prats, Exploring porous structures without crystals: advancements with pair distribution function in metal- and covalent organic frameworks, *Chem. Soc. Rev.*, 2024, **53**, 11772–11803, DOI: [10.1039/D4CS00267A](https://doi.org/10.1039/D4CS00267A).
15. L. Peng, Y. Peng, A. Primo and H. García, Porous Graphitic Carbons Containing Nitrogen by Structuration of Chitosan with Pluronic P123, *ACS Appl. Mater. Interfaces*, 2021, **13**, 13499–13507, DOI: [10.1021/acsami.0c19463](https://doi.org/10.1021/acsami.0c19463).
16. J. Panda, S. P. Tripathy, S. Dash, A. Ray, P. Behera, S. Subudhi and K. Parida, Inner transition metal-modulated metal organic frameworks (IT-MOFs) and their derived nanomaterials: a strategic approach towards

stupendous photocatalysis, *Nanoscale*, 2023, **15**, 7640–7675, DOI: [10.1039/D3NR00274H](https://doi.org/10.1039/D3NR00274H).

17 P. Behera, S. Subudhi, S. P. Tripathy and K. Parida, MOF derived nano-materials: a recent progress in strategic fabrication, characterization and mechanistic insight towards divergent photocatalytic applications, *Coord. Chem. Rev.*, 2022, **456**, 214392, DOI: [10.1016/j.ccr.2021.214392](https://doi.org/10.1016/j.ccr.2021.214392).

18 S. P. Tripathy, S. Subudhi and K. Parida, Inter-MOF hybrid (IMOFH): a concise analysis on emerging core–shell based hierarchical and multifunctional nanoporous materials, *Coord. Chem. Rev.*, 2021, **434**, 213786, DOI: [10.1016/j.ccr.2021.213786](https://doi.org/10.1016/j.ccr.2021.213786).

19 C. Fan, X. Gao, P. Tang, Q. Wang and B. Li, Molten Salt-Assisted Synthesis of Porous Precious Metal-Based Single-Atom Catalysts for Oxygen Reduction Reaction, *Adv. Sci.*, 2025, **12**, 2410784, DOI: [10.1002/advs.202410784](https://doi.org/10.1002/advs.202410784).

20 S. Mansingh, K. Kumar Das, R. Mohanty, N. Priyadarshini and K. Parida, Inverse opal type porous g-C<sub>3</sub>N<sub>4</sub> towards H<sub>2</sub>O<sub>2</sub> production and in-situ photoFenton gemifloxacin degradation driven by amorphous framework and nitrogen vacancy, *Appl. Catal., A*, 2025, **693**, 120141, DOI: [10.1016/j.apcata.2025.120141](https://doi.org/10.1016/j.apcata.2025.120141).

21 S. Patnaik, S. Martha and K. M. Parida, An overview of the structural, textural and morphological modulations of g-C<sub>3</sub>N<sub>4</sub> towards photocatalytic hydrogen production, *RSC Adv.*, 2016, **6**, 46929–46951, DOI: [10.1039/C5RA26702A](https://doi.org/10.1039/C5RA26702A).

22 B. P. Mishra and K. Parida, Orienting Z scheme charge transfer in graphitic carbon nitride-based systems for photocatalytic energy and environmental applications, *J. Mater. Chem. A*, 2021, **9**, 10039–10080, DOI: [10.1039/D1TA00704A](https://doi.org/10.1039/D1TA00704A).

23 D. P. Sahoo, K. K. Das, S. Patnaik and K. Parida, Double charge carrier mechanism through 2D/2D interface-assisted ultrafast water reduction and antibiotic degradation over architectural S,P co-doped g-C<sub>3</sub>N<sub>4</sub>/ZnCr LDH photocatalyst, *Inorg. Chem. Front.*, 2020, **7**, 3695–3717, DOI: [10.1039/D0QI00617C](https://doi.org/10.1039/D0QI00617C).

24 P. Dash, A. K. Kar, R. Srivastava and K. Parida, Harnessing mesoporous g-C<sub>3</sub>N<sub>4</sub>-based photocatalytic materials for sustainable fuel production *via* solar energy conversion: a review, *Mater. Horiz.*, 2025, **12**, 6485–6557, DOI: [10.1039/D5MH00294J](https://doi.org/10.1039/D5MH00294J).

25 S. Patnaik, B. P. Mishra and K. Parida, A review on dimensionally controlled synthesis of g-C<sub>3</sub>N<sub>4</sub> and formation of an isotype heterojunction for photocatalytic hydrogen evolution, *Catal. Sci. Technol.*, 2021, **11**, 7505–7524, DOI: [10.1039/D1CY01462E](https://doi.org/10.1039/D1CY01462E).

26 R.-H. Gao, Q. Ge, N. Jiang, H. Cong, M. Liu and Y.-Q. Zhang, Graphitic carbon nitride (g-C<sub>3</sub>N<sub>4</sub>)-based photocatalytic materials for hydrogen evolution, *Front. Chem.*, 2022, **10**, 1048504.

27 Y. Ba, W. Pan, S. Pi, Y. Zhao and L. Mi, Nitrogen-doped hierarchical porous carbon derived from a chitosan/polyethylene glycol blend for high performance supercapacitors, *RSC Adv.*, 2018, **8**, 7072–7079, DOI: [10.1039/C8RA00016F](https://doi.org/10.1039/C8RA00016F).

28 B. Chang, W. Shi, S. Han, Y. Zhou, Y. Liu, S. Zhang and B. Yang, N-rich porous carbons with a high graphitization degree and multiscale pore network for boosting high-rate supercapacitor with ultrafast charging, *Chem. Eng. J.*, 2018, **350**, 585–598, DOI: [10.1016/j.cej.2018.06.013](https://doi.org/10.1016/j.cej.2018.06.013).

29 G. Chu, C. Wang, Z. Yang, L. Qin and X. Fan, MOF-derived porous graphitic carbon with optimized plateau capacity and rate capability for high performance lithium-ion capacitors, *Int. J. Miner. Metall. Mater.*, 2024, **31**, 395–404, DOI: [10.1007/s12613-023-2726-2](https://doi.org/10.1007/s12613-023-2726-2).

30 M. E. Guye, M. D. Dabaro and H. Kim, Biomass-derived graphitic-like hierarchical porous carbon for electrochemical supercapacitor application, *J. Energy Storage*, 2025, **115**, 116037, DOI: [10.1016/j.est.2025.116037](https://doi.org/10.1016/j.est.2025.116037).

31 X. Zhu, L. Lin, M. Pang, C. Jia, L. Xia, G. Shi, S. Zhang, Y. Lu, L. Sun, F. Yu, J. Gao, Z. He, X. Wu, A. Li, L. Wang, M. Wang, K. Cao, W. Fu, H. Chen, G. Li, J. Zhang, Y. Wang, Y. Yang and Y.-G. Zhu, Continuous and low-carbon production of biomass flash graphene, *Nat. Commun.*, 2024, **15**, 3218, DOI: [10.1038/s41467-024-47603-y](https://doi.org/10.1038/s41467-024-47603-y).

32 V. Pusarapu, R. Narayana Sarma, P. Ochonma and G. Gadikota, Sustainable co-production of porous graphitic carbon and synthesis gas from biomass resources, *Npj Mater. Sustain.*, 2024, **2**, 16, DOI: [10.1038/s44296-024-00020-0](https://doi.org/10.1038/s44296-024-00020-0).

33 H. Liu, Z. Cui, Y. Sun, Z. Qiao, Y. Zhang, Q. Bai and Y. Wang, Synergistic design and synthesis of O, N Co-doped hierarchical porous carbon for enhanced supercapacitor performance, *Energy Mater.*, 2025, **5**, 500024, DOI: [10.20517/energymater.2024.101](https://doi.org/10.20517/energymater.2024.101).

34 Y. Zhao and X. Zhang, In situ activation graphitization to fabricate hierarchical porous graphitic carbon for supercapacitor, *Sci. Rep.*, 2021, **11**, 6825, DOI: [10.1038/s41598-021-85661-0](https://doi.org/10.1038/s41598-021-85661-0).

35 D. Xia, J. Mannering, P. Huang, Y. Xu, Q. Li, H. Li, Y. Qin, A. N. Kulak and R. Menzel, Electrothermal Transformations within Graphene-Based Aerogels through High-Temperature Flash Joule Heating, *J. Am. Chem. Soc.*, 2024, **146**, 159–169, DOI: [10.1021/jacs.3c06349](https://doi.org/10.1021/jacs.3c06349).

36 G. M. Laudone and K. L. Jones, A Grand Canonical Monte Carlo Simulation for the Evaluation of Pore Size Distribution of Nuclear-Grade Graphite from Kr Adsorption Isotherms, *C-J. Carbon Res.*, 2023, **9**, 86, DOI: [10.3390/c9030086](https://doi.org/10.3390/c9030086).

37 X. Liu, J. Choi, Z. Xu, C. P. Grey, S. Fleischmann and A. C. Forse, Raman Spectroscopy Measurements Support Disorder-Driven Capacitance in Nanoporous Carbons, *J. Am. Chem. Soc.*, 2024, **146**, 30748–30752, DOI: [10.1021/jacs.4c10214](https://doi.org/10.1021/jacs.4c10214).

38 G. Singh, A. Maria Ruban, H. Kaur, V. Patel, A. A. Ismaili, R. Bahadur and A. Vinu, High Surface Area Nanoporous Carbon-Ceria Composites for CO<sub>2</sub> Capture and Enzyme-Mimicking Action, *Chem.-An Asian J.*, 2024, **19**, e202400994, DOI: [10.1002/asia.202400994](https://doi.org/10.1002/asia.202400994).

39 N. C. Gallego, J. D. Arregui-Mena and C. I. Contescu, Probing basal planes and edge sites in polygranular nuclear graphite

by gas adsorption: Estimation of active surface area, *Carbon*, 2021, **179**, 633–645, DOI: [10.1016/j.carbon.2021.04.044](https://doi.org/10.1016/j.carbon.2021.04.044).

40 L. Zhang, C. Li and S. Pang, Dual-aromaticity in nitrogen-rich compounds: from fundamental concepts to the application of high-energy-density materials, *Coord. Chem. Rev.*, 2026, **546**, 217081, DOI: [10.1016/j.ccr.2025.217081](https://doi.org/10.1016/j.ccr.2025.217081).

41 S.-S. Wang, C.-H. Hsu, C.-T. Tsai, H.-P. Lin, C.-W. Yan, J.-K. Chang, T.-H. Hsieh, C.-W. Huang and C.-H. Lee, Conversion of wood waste into nitrogen-doped graphite-like multiporous carbon with high specific surface area and electrical conductivity for high-voltage supercapacitors, *Sustain. Energy Fuels.*, 2025, **9**, 2355–2368, DOI: [10.1039/D4SE01603C](https://doi.org/10.1039/D4SE01603C).

42 M. Martincic, S. Sandoval, J. Oró-Solé and G. Tobías-Rossell, Thermal Stability and Purity of Graphene and Carbon Nanotubes: Key Parameters for Their Thermogravimetric Analysis (TGA), *Nanomaterials*, 2024, **14**, 1754, DOI: [10.3390/nano14211754](https://doi.org/10.3390/nano14211754).

43 C. Chen, D. Yu, G. Zhao, L. Sun, Y. Sun, K. Leng, M. Yu and Y. Sun, Hierarchical porous graphitic carbon for high-performance supercapacitors at high temperature, *RSC Adv.*, 2017, **7**, 34488–34496, DOI: [10.1039/C7RA06234F](https://doi.org/10.1039/C7RA06234F).

44 P. V. Polyakova and J. A. Baimova, Mechanical Properties of Graphene Networks under Compression: A Molecular Dynamics Simulation, *Int. J. Mol. Sci.*, 2023, **24**(7), 6691, DOI: [10.3390/ijms24076691](https://doi.org/10.3390/ijms24076691).

45 M. Jalalah, H. Han, A. K. Nayak and F. A. Harraz, High-performance supercapacitor based on self-heteroatom-doped porous carbon electrodes fabricated from Mikania micrantha, *Adv. Compos. Hybrid Mater.*, 2024, **7**, 20, DOI: [10.1007/s42114-024-00833-6](https://doi.org/10.1007/s42114-024-00833-6).

46 Y. N. Yusoff, S. Norazuwana, R. Nor Fatina, M. Mohamad Azuwa, K. Siti Kartom, L. Kee Shyuan, H. Roshasnorlyza and A. Ahmad Wani, Enhanced specific surface area in 2D graphitic carbon nitride nanosheets *via* two-step calcination temperature-induced structural transformation, *Chem. Eng. Commun.*, 1–11, DOI: [10.1080/00986445.2025.2461634](https://doi.org/10.1080/00986445.2025.2461634).

47 W.-Y. Park, J. Han, J. Moon, S.-H. Joo, T. Wada, Y. Ichikawa, K. Ogawa, H. S. Kim, M. Chen and H. Kato, Mechanically Robust Self-Organized Crack-Free Nanocellular Graphene with Outstanding Electrochemical Properties in Sodium Ion Battery, *Adv. Mater.*, 2024, **36**, 2311792, DOI: [10.1002/adma.202311792](https://doi.org/10.1002/adma.202311792).

48 B. Chang, Y. Guo, Y. Li, H. Yin, S. Zhang, B. Yang and X. Dong, Graphitized hierarchical porous carbon nanospheres: simultaneous activation/graphitization and superior supercapacitance performance, *J. Mater. Chem. A*, 2015, **3**, 9565–9577, DOI: [10.1039/C5TA00867K](https://doi.org/10.1039/C5TA00867K).

49 L. Liu, Y. Wu, H. Wang, X. Yang, W. Zhu, S. Ma, X. Lu, Y. Li, P. Ren, P. Yang and R. Li, Pore-edge graphitic nitride-dominant hierarchically porous carbons for boosting oxygen reduction catalysis, *Sustain. Energy Fuels.*, 2024, **8**, 2050–2058, DOI: [10.1039/D4SE00135D](https://doi.org/10.1039/D4SE00135D).

50 L. A. M. Mahmoud, J. L. Rowlandson, D. J. Fermin, V. P. Ting and S. Nayak, Porous carbons: a class of nanomaterials for efficient adsorption-based hydrogen storage, *RSC Appl. Interfaces.*, 2025, **2**, 25–55, DOI: [10.1039/D4LF00215F](https://doi.org/10.1039/D4LF00215F).

51 Z. Zhou, K. Zhao, H.-Y. Chi, Y. Shen, S. Song, K.-J. Hsu, M. Chevalier, W. Shi and K. V. Agrawal, Electrochemical-repaired porous graphene membranes for precise ion-ion separation, *Nat. Commun.*, 2024, **15**, 4006, DOI: [10.1038/s41467-024-48419-6](https://doi.org/10.1038/s41467-024-48419-6).

52 C. Francis, A. Rektor, T. Valayil-Varghese, N. McKibben, I. Estrada, J. Forbey and D. Estrada, Laser-induced graphene gas sensors for environmental monitoring, *Front. Chem.*, 2024, **12**, 1448205, DOI: [10.3389/fchem.2024.1448205](https://doi.org/10.3389/fchem.2024.1448205).

53 Q. Zhang, S. Chen, H. Chen, Y. Hu and Q. Lin, A novel oxidized hierarchical porous carbon with vesicule-like ultrathin graphitic walls for efficient removal of anionic and cationic dyes, *Environ. Res.*, 2025, **267**, 120702, DOI: [10.1016/j.envres.2024.120702](https://doi.org/10.1016/j.envres.2024.120702).

54 K. Sattari, L. Eddy, J. L. Beckham, K. M. Wyss, R. Byfield, L. Qian, J. M. Tour and J. Lin, A scientific machine learning framework to understand flash graphene synthesis, *Digit. Discov.*, 2023, **2**, 1209–1218, DOI: [10.1039/D3DD00055A](https://doi.org/10.1039/D3DD00055A).

55 J. T. Davis, B. S. Jayathilake, S. Chandrasekaran, J. J. Wong, J. R. Deotte, S. E. Baker, V. A. Beck, E. B. Duoss, M. A. Worsley and T. Y. Lin, 3D printed optimized electrodes for electrochemical flow reactors, *Sci. Rep.*, 2024, **14**, 22662, DOI: [10.1038/s41598-024-71765-w](https://doi.org/10.1038/s41598-024-71765-w).

56 K. Coe-Sessions, A. E. Davies, B. Dhokale, M. J. Wenzel, M. Mahmoudi Gahrouei, N. Vlastos, J. Klaassen, B. A. Parkinson, L. D. S. Oliveira and J. O. Hoberg, Functionalized Graphene *via* a One-Pot Reaction Enabling Exact Pore Sizes, Modifiable Pore Functionalization, and Precision Doping, *J. Am. Chem. Soc.*, 2024, **146**, 33056–33063, DOI: [10.1021/jacs.4c10529](https://doi.org/10.1021/jacs.4c10529).

57 Z. Amjad, A. P. Terzyk and S. Boncel, Covalent functionalization of 1D and 2D sp<sub>2</sub>-carbon nanoallotropes – twelve years of progress (2011–2023), *Nanoscale*, 2024, **16**, 9197–9234, DOI: [10.1039/D3NR06413A](https://doi.org/10.1039/D3NR06413A).

58 Y. Yu, Y. Zhang, Y. Zhou, J. Xia, M. Chen, H. Fu, Y. Cao, T. Wang, C. Wu, Z. Luo and Y. Zhang, Enhanced Electromagnetic Interference Shielding Properties of CNT/Carbon Composites by Designing a Hierarchical Porous Structure, *Nanomaterials*, 2024, **14**(13), 1099, DOI: [10.3390/nano14131099](https://doi.org/10.3390/nano14131099).

59 X. Wang, L. Li, Y. Lin, J. Xu, J. Zhao, X. Zhang, F. Wang and X. Wang, Methane Hydrates Formed in a Porous Graphene Aerogel for Energy Storage, *Cryst. Growth Des.*, 2024, **24**, 9223–9234, DOI: [10.1021/acs.cgd.4c01220](https://doi.org/10.1021/acs.cgd.4c01220).

60 S. M. S. Shahriar, A. D. McCarthy, S. M. Andrabi, Y. Su, N. S. Polavoram, J. V. John, M. P. Matis, W. Zhu and J. Xie, Mechanically resilient hybrid aerogels containing fibers of dual-scale sizes and knotty networks for tissue regeneration, *Nat. Commun.*, 2024, **15**, 1080, DOI: [10.1038/s41467-024-45458-x](https://doi.org/10.1038/s41467-024-45458-x).

61 Q. Liu and X. Li, Molten salt synthesis of porous grapheme-like carbons as peroxydisulfate catalyst for the efficient

removal of rhodamine B dye, *Environ. Sci. Pollut. Res.*, 2024, **31**, 43249–43261, DOI: [10.1007/s11356-024-33951-1](https://doi.org/10.1007/s11356-024-33951-1).

62 C. Wang, X. Cheng, K. H. Luo, K. Nandakumar, Z. Wang, M. Ni, X. Bi, J. Zhang and C. Wang, A guided review of machine learning in the design and application for pore nanoarchitectonics of carbon materials, *Mater. Sci. Eng., R*, 2025, **165**, 101010, DOI: [10.1016/j.mser.2025.101010](https://doi.org/10.1016/j.mser.2025.101010).

63 H. Liu, S. Su, H. Wang, M. Wang, S. Zhang, B. Chang and B. Yang, A sustainable one-step strategy for highly graphitized capacitive carbons with hierarchical micro-meso-macro porosity, *Nanoscale Adv.*, 2022, **4**, 1394–1407, DOI: [10.1039/D1NA00856K](https://doi.org/10.1039/D1NA00856K).

64 W. Shi, B. Chang, H. Yin, S. Zhang, B. Yang and X. Dong, Crab shell-derived honeycomb-like graphitized hierarchically porous carbons for satisfactory rate performance of all-solid-state supercapacitors, *Sustain. Energy Fuels.*, 2019, **3**, 1201–1214, DOI: [10.1039/C8SE00574E](https://doi.org/10.1039/C8SE00574E).

65 S. Liu, Q. Zhang, J. Liu, J. Li, W. Liu, Y. Wang and S. Yuan, Nitrogen-Doped Porous Carbons Derived from Peanut Shells as Efficient Electrodes for High-Performance Supercapacitors, *Int. J. Mol. Sci.*, 2024, **25**(14), 7583, DOI: [10.3390/ijms25147583](https://doi.org/10.3390/ijms25147583).

66 Y. Wu, H. Tang, L. Kang, H. Li and N. Jiang, A Two-Layer Graphene Nonwoven Fabric for Effective Electromagnetic Interference Shielding, *Materials*, 2024, **17**(15), 3747, DOI: [10.3390/ma17153747](https://doi.org/10.3390/ma17153747).